ACS OMEGA

http://pubs.acs.org/journal/acsodf
Article

In Situ Monitoring and Estimation of α-Lactose Monohydrate Crystal Growth in the Microdroplets

Youliang Guan, Yanqin Cai, Jingqin Jiang, and Zujin Yang*

Cite This: ACS Omega 2025, 10, 10493−10505

Read Online

ACCESS | Metrics & More | Article Recommendations | Supporting Information

ABSTRACT: In this study, a new microfluidic chip that generates microscale emulsion droplets to confine α-lactose monohydrate crystal (α-LM) solutions in the microdroplets was used to prepare uniform-sized crystals. In situ observations for α-LM growth were performed by using a dual-camera structured light system consisting of two cameras fixed at different angles, achieving a satisfactory three-dimensional (3D) shape reconstruction. After 3D shape reconstruction from image processing, the 3D axial size, crystal surface area, and volume of α-LM in the microdroplets were measured at different time intervals. By fitting these data, we could quantitatively estimate 3D axial growth rates, real-time concentration, and supersaturation (σ) of α-LM. The experimental results show that the growth rate of α-LM from aqueous solution is the fastest in the nucleated 100−150 min after nucleation, and the particle volume of α-LM is about 7.08×10^{-6} cm^3 at $\sigma = 1.5$. The fitted polynomial coefficients show that the growth processes of α-LM in the microdroplets are mainly between second-order growth and fourth-order growth. The nucleation and growth mechanisms of α-LM in microdroplets are also clarified. In general, the real-time monitoring of α-LM growth in the microdroplets could avoid interference and damage to the crystals from various impurities and external forces, maintaining the characteristics of the natural growth of the crystals. The results demonstrate the applicability of the proposed method by correctly predicting the experimental morphologies of α-LM grown from the solutions.

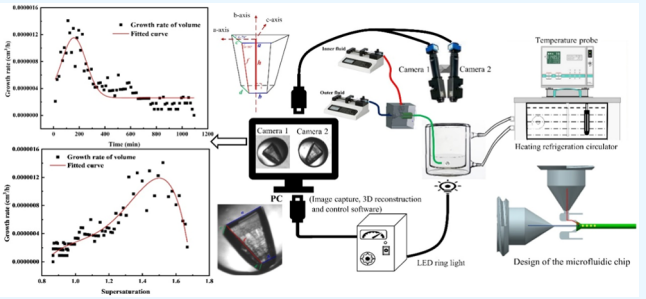

1. INTRODUCTION

Solution crystallization is an ideal strategy for separating different components from solutions and purifying particle products in the food industry. Lactose (4-O-β-D-galactopyranosyl-D-glucopyranose, $C_{12}H_{22}O_{11}$) is a milk disaccharide, which is composed of D-galactose and D-glucose linked by a β-1,4 glycosidic linkage. It is mainly produced from whey solutions, and it has been extensively applied in the food and pharmaceutical industries due to its low caloric value, glycemic response, and sweetness.[1−3] Lactose is usually present in the two isomeric forms in solution, α-lactose and β-lactose, through the mutarotation reaction. α-LM can be recovered from a supersaturated solution by controlling the crystallization kinetics, which is a key factor in affecting the morphology of crystals. Hayashi et al.[4] reported growth rates of NaCl whiskers in an aqueous solution in 1974. Kurihara et al.[5] measured the normal growth rates of protein crystals with surface supersaturation by considering concentration distribution around growing crystals using a two-beam interferometer, implying that the growth was regulated by two-dimensional nucleation. However, the process is influenced by external conditions, including organic acids, salts, and other substances. They can form different morphologies, such as needle-like, rod-shaped, and tomahawk-shaped crystal sizes.[6−8] Dombrowski et al.[9] developed a microfluidic process to produce α-LM by confining the crystals in droplets through a T-type microfluidic chip, and the crystals with narrower crystal size distribution (CSD) were observed with the coefficient of change of crystal size as low as 7%. Parimaladevi et al.[10] reported a novel swift cooling crystallization process to produce α-LM in a shorter induction period, and the interfacial energy played an important role in producing crystals with a regular shape, low defect density, and neat internal arrangement. Dincer et al.[11] measured the growth rates and growth rate dispersion (GRD) of four different faces of α-LM in the temperature range of 30−50 °C and in the relative supersaturation σ range of 0.55−2.33 in aqueous solutions, where σ is the difference between the actual concentration and the saturation concentration.[12] However, these methods could not in situ monitor the crystallization process to effectively control the size and shape of α-LM. In order to optimize the crystallization process, online analytical technologies (PATs) have been used to evaluate the morphology, growth rate, and product quality of the crystals.[13−15] Currently, online and real-time character-

Received: November 28, 2024
Revised: February 19, 2025
Accepted: February 26, 2025
Published: March 7, 2025

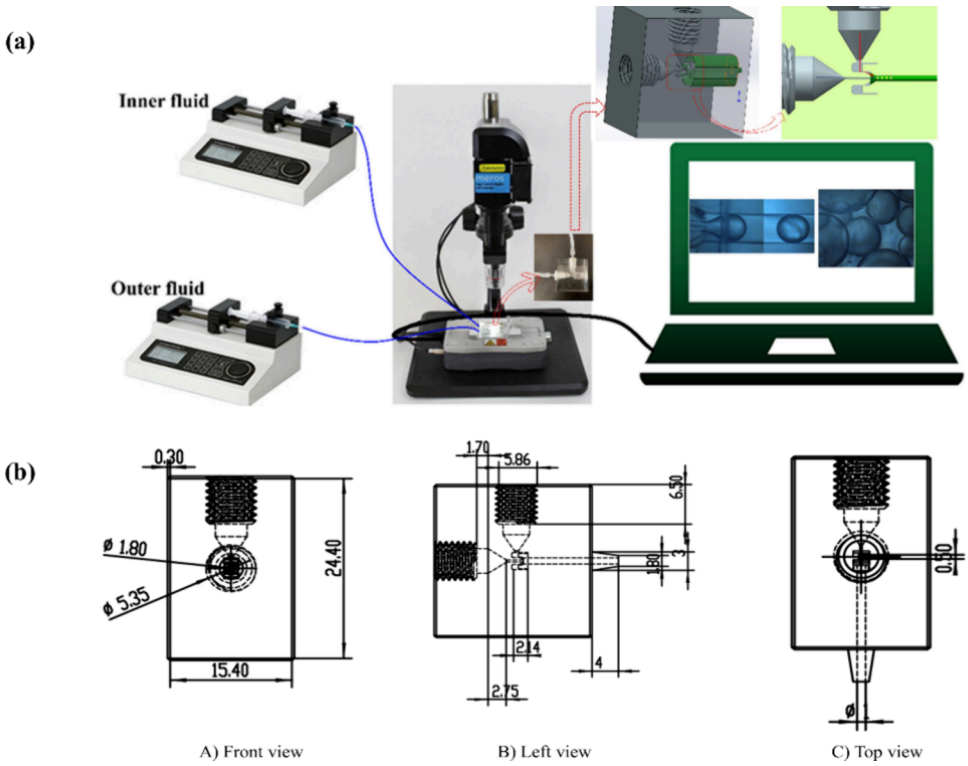

Figure 1. Schematic diagram of the preparation of W/O droplets (a) and structure and size of the microfluidic chip (b).

ization of crystal size and shape is mostly focused-beam reflectance measurement (FBRM) based on laser light backscattering and measures particle cord length distribution (CLD). CLD is a method for measuring and analyzing particle size distribution,[16−18] but there exists a large error if the morphology of the crystal is far away from the spherical shape. To overcome these issues, microscopy imaging has been used to measure the particle shape. However, there is a significant error between the size and shape of the crystals measured and the actual size and shape using 2D images, which is due to the continuous rotation and movement of the crystals in the crystallization process.[19,20] Zhang et al.[21] proposed a 2D imaging technique to assess the estimated needle-like and rod-shaped crystal size, and the predicted values were reduced by approximately 67% compared to the actual sizes. To measure the shape and size of the crystals more precisely, Jin et al.[22] applied a 3D face reconstruction framework to replace the traditional 2D images, which was performed by a stereo camera model using two cameras fixed at the optimal angle and synchronously taking images. The images of objects seen by the left and right eyes are slightly different, but the brain can combine the left and right images to calculate the real 3D images.

Recently, microfluidic technology has received considerable attention due to its obvious advantages, such as low sample reagent consumption, low mass production costs, short analysis time, high dimensional accuracy, and high sensitivity detection.[23−25] It is widely used in the food, pharmaceutical, and cosmetics industries, especially microfluidics have been used to prepare solid particles, core−shell microcapsules, and multichamber microcapsules.[26−28] However, the application of microfluidic technology for controlling crystal nucleation and growth, as well as monitoring the crystal crystallization process, combining an in situ imaging system, has been rarely reported.

The aim of the present work is to design and synthesize an efficient and confocal microfluidic device for the preparation of α-LM droplets. The crystallization conditions to control the crystallization of α-LM in the microcapsules were optimized, and the nucleation−growth kinetic equations under constrained conditions were investigated in detail.

2. MATERIALS AND METHODS

2.1. Materials. α-LM (purity, ≥ 99%) was purchased from Sigma-Aldrich (St. Louis, MO, USA). Kerosene was obtained from the Damao Chemical Reagent Factory (Tianjin, China). Deionized (DI) water was obtained with a Milli-Q water system (Resistivity: 18.3 MΩ·cm) and used to prepare the sample solutions. All chemicals were of analytical grade and used as received without further purification.

2.2. Design and Fabrication of a Microchannel Chip. 3D software modeling was used to complete component assembly and integration based on bottom-up design ideas. The schematic diagram of the as-prepared microchannel chip is shown in Figure 1a. The continuous and dispersed phases are fed through the threaded external Luer straight-through connector of the chip and inner diameter of the silicone hose (1.0 mm), and then the generated droplets are collected into the beaker through the external hose. The designed chip structure and size are shown in Figure 1b, and poly(methyl methacrylate) (PMMA) is used as the base material. After plane treatment, the processed PMMA with symmetrical channels was further bonded and encapsulated with the help of a computer numerical control (CNC) milling machine, which was used to prepare water/oil (W/O) droplets.

2.3. Preparation of W/O and α-LM Droplets. Based on the fabrication of the microfluidic chips and the flow characteristics of W/O droplets, the nucleation zone of α-LM in aqueous solution was measured according to the

https://doi.org/10.1021/acsomega.4c10746
ACS Omega 2025, 10, 10493−10505

previous refs 29,30. The solubility of α-LM in water at 60 and 25 °C was determined to be 58.87 g/100 g ($w_{\alpha\text{-LM}}$ = 37.06%) and 22.03 g/100 g ($w_{\alpha\text{-LM}}$ = 22.03%), respectively.

In this study, the two-phase system is mostly made up of kerosene and water. DI water was used as the dispersion phase, and kerosene was selected as the continuous phase. A high-speed camera was used to observe and record the droplet formation process and flow in the microchannel chip. Then, the W/O droplets were prepared by exchanging the interface between the dispersed phase and the continuous phase in the device (Figure 1a). α-LM droplets were also prepared according to the previous method,[29] with minor modifications. Typically, 58.87 g of α-LM was dissolved in 100 mL of DI water at 60 °C and filtered through a 0.45 μm PTFE syringe filter to obtain a saturated aqueous solution, which was used as a dispersion phase (flow rate: 1 mL/h) and injected into the custom-made chip. Then, kerosene was used as the continuous phase (flow rate: 60 mL/h). Under the shear action of kerosene, some stable and uniform sized α-LM droplets (diameter of about 550 μm) were generated, flowed into a jacketed beaker through silicone tubes (diameter of about 1000 μm), and mixed with 50 mL of kerosene at different constant temperatures. By rotating the bracket and adjusting the angle of the light source and camera, both lenses were simultaneously focused on the same droplet, and the nucleation and growth of α-LM in the beaker were observed constantly, performing a series of experiments as summarized in the Supporting Information (Figure S1). We performed a comprehensive inspection and calibration to the microscope equipment and further optimized the shooting parameters, such as the aperture, shutter speed, sensitivity, etc., to ensure that a clear image was acquired every time. In addition, we combined the autofocus function with manual fine-tuning to confirm the focus position multiple times, preventing photos from being out-of-focus. To ensure the reliability of in situ observation, it is necessary to control the number of α-LM molecules in the droplets. In this study, by adjusting the flow rate of the internal and external phases, the number of crystals can be controlled in the droplets, which is used to observe the nucleation and growth of α-LM.

In the present study, 3D shape reconstruction was applied to replace the traditional 2D imaging with two cameras fixed at the best angle and shooting images synchronously, and the 3D reconstruction of the crystal shape was carried out as shown in the Supporting Information (Figure S2). The imaging steps for reconstructing the 3D shape of the crystals mainly included inflection point detection, feature extraction, image processing, matching constraints, coordinate transformation, crystal rotation, 3D shape reconstruction, and stereoimmunization of two sets of photos, all of which were used to estimate and calculate the crystal face growth, achieving the crystal growth dynamics.

2.4. Stereoscopic Imaging Camera Model. Stereoscopic imaging is similar to the 3D vision of the human eye. The two eyes are about 7 cm apart. The images of the objects seen by the left and right eyes are slightly different, but the brain combines the left and right images to calculate the real 3D image. In the present study, two synchronous cameras arranged at the best angles are used to capture 2D images containing 3D information on α-LM crystals. The most common camera model used for 3D reconstruction is the pinhole-camera model (PM). Before describing the camera model of stereo imaging, PM was introduced as,

The point with coordinate $\boldsymbol{X} = (X, Y, Z)^{\mathrm{T}}$ in 3D space is mapped to the point X with coordinate $(fX/Z, fY/Z, f)^T$ on a 2D plane. When the points from the object and the image are represented by a homogeneous vector, the above projection can be roughly expressed as a matrix multiplication between their homogeneous coordinates and the linear mapping associated with these two sets of coordinates, which can be determined as eq 1,

$$\begin{pmatrix} X \\ Y \\ Z \\ 1 \end{pmatrix} + \begin{pmatrix} fX \\ fY \\ Z \end{pmatrix} = \begin{bmatrix} f & & & 0 \\ & f & & 0 \\ & & 1 & 0 \end{bmatrix} \begin{pmatrix} X \\ Y \\ Z \\ 1 \end{pmatrix} \tag{1}$$

However, the relationship between the points in 3D space and the corresponding points on the image may be much more complex than the above linear mapping, and the camera model can be defined as eq 2,

$$\begin{pmatrix} X' \\ Y' \\ Z' \end{pmatrix} = \begin{pmatrix} P_{11} & P_{12} & P_{13} & P_{14} \\ P_{21} & P_{22} & P_{23} & P_{24} \\ P_{31} & P_{32} & P_{33} & P_{34} \end{pmatrix} \begin{pmatrix} X \\ Y \\ Z \\ 1 \end{pmatrix} = P \begin{pmatrix} X \\ Y \\ Z \\ 1 \end{pmatrix} \tag{2}$$

In eq 2, the matrix P is called the calibration matrix of the camera, including the internal and external parameters of the camera. The 2D projection can be obtained by projecting the 3D polyhedron shape onto the plane and ensuring that the origin of the image coordinate system is the principal point so that the object coordinate system is the same as the camera coordinate system, ignoring the distortion of the camera lens. eq 2 can be used directly as a camera model because it affects only the size of the transformed image, not its shape. In this work, all of the spatial coordinates are first converted to the Cartesian coordinate system, which can be calculated by rotating the crystal.

2.5. 3D Shape of a Digital Crystal. The 3D shape of a crystal consists of faces, edges, and vertices. Two faces intersect to produce edges, and three or more faces intersect to produce vertices. In the study, we studied the three-dimensional size evolution of α-LM crystals and focused on the contour vertices. When all of the vertex coordinates (V matrix) were obtained, the shape of the crystal was known. The coordinate matrix of the vertices in the crystal space can be expressed as eq 3,

$$V = N^{-1}H \tag{3}$$

In eq 3, V is a 3 × 1 spatial coordinate vector, and N is an n × 3 matrix with n plane normal. The unit normal n of the plane can be calculated from the crystal axis and Miller index of the crystal system, and H is an n × 1 matrix including the normal distance of each plane.

When all the spatial coordinates are converted to the Cartesian coordinate system, rotating the 3D crystal in the camera model is the same as rotating the reference frame along the Euler angles δ, θ, and φ. The vertex (P_i matrix) of the crystal projection on the corresponding 2D plane can be obtained by multiplying the vertex coordinate matrix V with the camera calibration matrix P, as shown in eqs 4 and 5),

$$P_i = P \times V \tag{4}$$

https://doi.org/10.1021/acsomega.4c10746
ACS Omega 2025, 10, 10493−10505

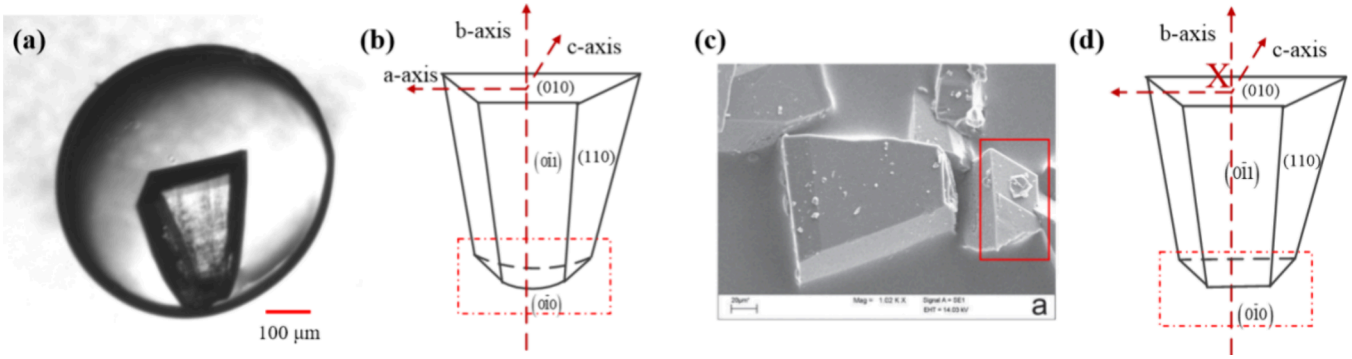

Figure 2. Morphology of α-LM: formation in microdroplets (a), schematic diagram of Miller index with a curved surface at the top (b), SEM image of α-LM in the previous ref 31 (c), and the shape of the prism obtained by approximate treatment with a plane at the top (d).

$$P = P_1P_2 = \begin{bmatrix}1 & 0 & 0\\ 0 & 1 & 0\end{bmatrix} \times \begin{bmatrix}\cos\delta & -\sin\delta & 0\\ \sin\delta & \cos\delta & 0\\ 0 & 0 & 1\end{bmatrix} \times \begin{bmatrix}1 & 0 & 0\\ 0 & \cos\theta & -\sin\theta\\ 0 & \sin\theta & \cos\theta\end{bmatrix} \times \begin{bmatrix}\cos\varphi & -\sin\varphi & 0\\ \sin\varphi & \cos\varphi & 0\\ 0 & 0 & 1\end{bmatrix} \quad (5)$$

To ensure that the rotating crystal contains as many directions as possible and the probability is equal, the values of δ, θ, and φ satisfy the inequality 6, and can be selected randomly as eq 6,

$$0 \le \delta < 2\pi;\ 0 \le \varphi < 2\pi;\ \theta = \arcsin(\sigma),\ -1 \le \sigma < 1 \quad (6)$$

To better match the projected image in the database and the in situ growth image captured by the camera, the camera model is used to generate two databases for two virtual cameras. When the grains are observed from the Z axis of the rotation coordinates and the two databases have the same δ and φ, the difference of the rotation angle between the two databases comes from θ. In addition, the related properties of the projection need to be calculated according to the vertices of the crystal, such as area An and centroid coordinates (X_c, Y_c), which can be calculated by using the coordinates and formulas of n_j vertices in the crystal profile 7 and 9, respectively, because the adjacent vertices are connected to form the boundary of the crystal projection.

$$A = \frac{1}{2}\sum_{i=1}^{n_j}(X_iY_{i+1} - X_{i+1}Y_i) \quad (7)$$

$$X_c = \frac{1}{2}\sum_{i=1}^{n_j}(X_i + X_{i+1})(X_iY_{i+1} - X_{i+1}Y_i) \quad (8)$$

$$Y_c = \frac{1}{2}\sum_{i=1}^{n_j}(Y_i + Y_{i+1})(X_iY_{i+1} - X_{i+1}Y_i) \quad (9)$$

3. RESULTS AND DISCUSSION

3.1. Effect of the Internal Phase Fluid Flow Rate on W/O Droplets. When the external phase flow rate is set at Q_{out} = 10 mL/h and the internal phase flow rate (Q_{in}) rises from 1 to 20 mL/h, the diameter of the generated droplets increases gradually with decreasing shear force exerted by the continuous phase to dispersed phase. When Q_{in} > 6 mL/h, the diameter of the droplet is larger than that of the tube, generating rod-shaped droplets due to the limited tube space. In addition, the droplets may transform from a trickle break at low internal phase flow rates to jet flow fracture at high internal phase flow rates with the increase of Q_{in} (Figure S3, Supporting Information). The growth conditions for enhanced crystallization of microdroplets are (a) in the early stage of droplet formation, the vortices generated inside the droplet can significantly improve its mass transfer performance, and the mass transfer coefficient is 10−100 times quicker than that of the droplet movement stage, which was possibly caused by the flow pattern within the droplet during the formation stage; (b) microdroplets have a large specific surface area, which increases the interfacial area, improves the nonuniformity of multiphase mixing, and significantly enhances mass transfer efficiency.

3.2. Effect of the External Phase Flow Rate on W/O Droplets. When the internal phase flow rate is set at Q_{in} = 1 mL/h and the external phase flow rate (Q_{out}) increases from 2 to 50 mL/h, the diameter of the generated droplets decreases significantly with increasing the shear force exerted by the continuous phase fluid to dispersed phase fluid. The droplet changes from the extrusion fracture at low external phase velocity to the trickle fracture at high external phase velocity with the increase of Q_{out} (Figure S4, Supporting Information). Under the extrusion mechanism, the size of the droplet is larger than that of the channel, which is deformed into a flat shape in the channel.

3.3. Approximate Treatment of Crystal Morphology. The morphology of the α-LM obtained in this study is similar to the previous result,[29] which is just a trimmed version of the tomahawk shape, as shown in Figure 2a. And the corresponding crystal plane index is shown in Figure 2b, which has a curved surface at the top. The previous results show that the crystal plane (010) of α-LM is a trapezoid (Figure 2c).[24,31] For the convenience of 3D reconstruction and data processing, the crystal plane (0$\bar{1}$0) is approximated as a trapezoid with the same shape as the crystal plane (010). The approximate prism shape is very close to the original crystal size, which significantly reduces the impact of data processing to a minimum (Figure 2d), and X represents the coordinate origin of the reconstructed 3D crystal (0, 0, 0).

The growth of α-LM can be considered to occur layer by layer, so the molecules in the solution must be desolvated and adsorbed on the crystal surface to form each layer.[32] The

https://doi.org/10.1021/acsomega.4c10746
ACS Omega 2025, 10, 10493−10505

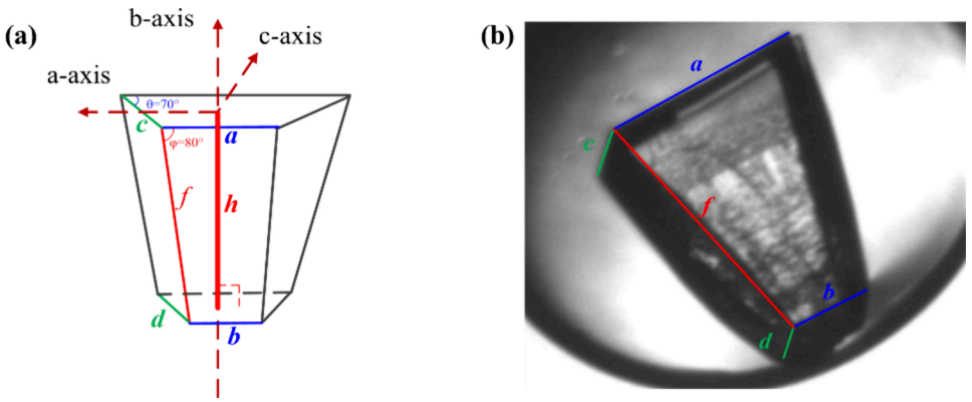

Figure 3. Crystal edge comparison in 3D reconstruction of α-LM. Schematic diagram (a); actual photo (b).

empirical eq 10 is often used to describe the crystal growth rate in the actual process.[33]

$$G = k\sigma^n \tag{10}$$

In the equation, G is the crystal growth rate, k is the growth rate constant, σ represents supersaturation, and n is the growth order.

3.4. Calculation of Real-Time Supersaturation in Microdroplets. The spatial coordinate system and crystal-related dimensions required in the calculation process of the 3D reconstruction of α-LM are shown in Figure 3. The size change of crystal prism a represents the growth of α-LM in the axis of a. The growth of α-LM in the b-axis direction ($h = f \times \sin 80°$) means the change of the bevel height h, and the growth of α-LM in the c-axis direction is the change of trapezoidal height (010) trapezoidal height ($c \times \sin 70°$). In this study, the growth trend of α-LM was expressed by the growth of crystal plane areas and crystal volumes.

After image processing and 3D reconstruction, the crystal edge size was determined and the growth trend of each dimension of α-LM could be calculated. According to the previous ref 34, the densities of α-LM aqueous solution ($w_{\alpha\text{-LM}}$ = 37.06%) and α-LM crystal are 1.1668 and 1.54 g/cm^3, respectively. Combined with the changes in real-time concentration ($w_{\alpha\text{-LM}}^{\text{real}}$) and σ of α-LM, the growth kinetics of α-LM could be obtained. In order to acquire clear mathematical relations and mathematical constants, the calculation process could be written as eqs 11−17, and trapezoidal area S was (upper + bottom) × height/2.

The area of crystal plane (010), which is the area of the top trapezoid, is calculated as eq 11,

$$S_{(010)} = (ac + c^2 \cos 70°) \sin 70° \tag{11}$$

The area of crystal face $(0\bar{1}0)$, that is, the area of the bottom trapezoid, is calculated as eq 12,

$$S_{(0\bar{1}0)} = (bd + d^2 \cos 70°) \sin 70° \tag{12}$$

The area of crystal face $(0\bar{1}1)$, that is, the area of the intermediate trapezoid, is calculated as eq 13,

$$S_{(0\bar{1}1)} = \frac{1}{2}(a + b)(f \sin 80°) \tag{13}$$

The volume of the entire crystal, V_{crystal}, is calculated by eq 14,

$$V_{\text{crystal}} = \frac{h}{3}\left(S_{(010)} + S_{(0\bar{1}0)} + \sqrt{S_{(010)}S_{(0\bar{1}0)}}\right) \tag{14}$$

The volume of the inner cavity (sphere) of the micro-droplets (inner diameter is $D \approx 567$ μm), V_{sphere} is calculated as eq 15,

$$V_{\text{sphere}} = \frac{\pi D^3}{6} \tag{15}$$

The real-time concentration of α-LM aqueous solution in the droplets = (total mass of α-LM − mass of precipitated crystals)/mass of water in the droplets, $w_{\alpha\text{-LM}}^{\text{real}}$ is calculated as eq 16,

$$w_{\alpha\text{-LM}}^{\text{real}} = \frac{m_{\alpha\text{-LM}}^{\text{all}} - m_{\alpha\text{-LM}}^{\text{real}}}{m_{\text{H}_2\text{O}}} = \frac{V_{\text{sphere}} \times \rho_{\alpha\text{-LM/H}_2\text{O}} \times w_{\alpha\text{-LM}} - V_{\text{crystal}} \times \rho_{\alpha\text{-LM}}}{V_{\text{sphere}} \times \rho_{\alpha\text{-LM/H}_2\text{O}} \times (1 - w_{\alpha\text{-LM}})} \tag{16}$$

Real-time supersaturation σ of α-LM aqueous solution in droplets is calculated as eq 17,

$$\sigma = \frac{w_{\alpha\text{-LM}}^{\text{real}} - 0.2203}{0.2203} \tag{17}$$

3.5. In Situ Growth and 3D Reconstruction of α-LM Crystals. As shown in Figure 4, the in situ nucleation−growth process of α-LM was recorded simultaneously from both directions using dual cameras to study the kinetic process. The field from the view of an industrial camera is a 3070 × 2460 μm true area calibrated by a 500 μm ruler. The image acquisition software is the OPT Camera Demo provided by Dongguan OPT, which was set to collect 1 picture with a resolution of 1280 × 1024 pixels per minute. Image processing software PIAE (Process Image Analysis Expert) mainly has edge recognition, crystal segmentation, and other functions based on MATLAB software. In order to reduce the amount of calculation in the reconstruction process, one pair of photos was selected every 14 min from more than 1100 pairs of photos taken for data processing. The moving window approach was used to calculate various growth rates. The growth rates at moments 2 and 3 are ($L_{\text{moment 2}} - L_{\text{moment 1}}$)/time interval and ($L_{\text{moment 3}} - L_{\text{moment 2}}$)/time interval, respectively. L represents the crystal size at the corresponding moment.

https://doi.org/10.1021/acsomega.4c10746
ACS Omega 2025, 10, 10493−10505

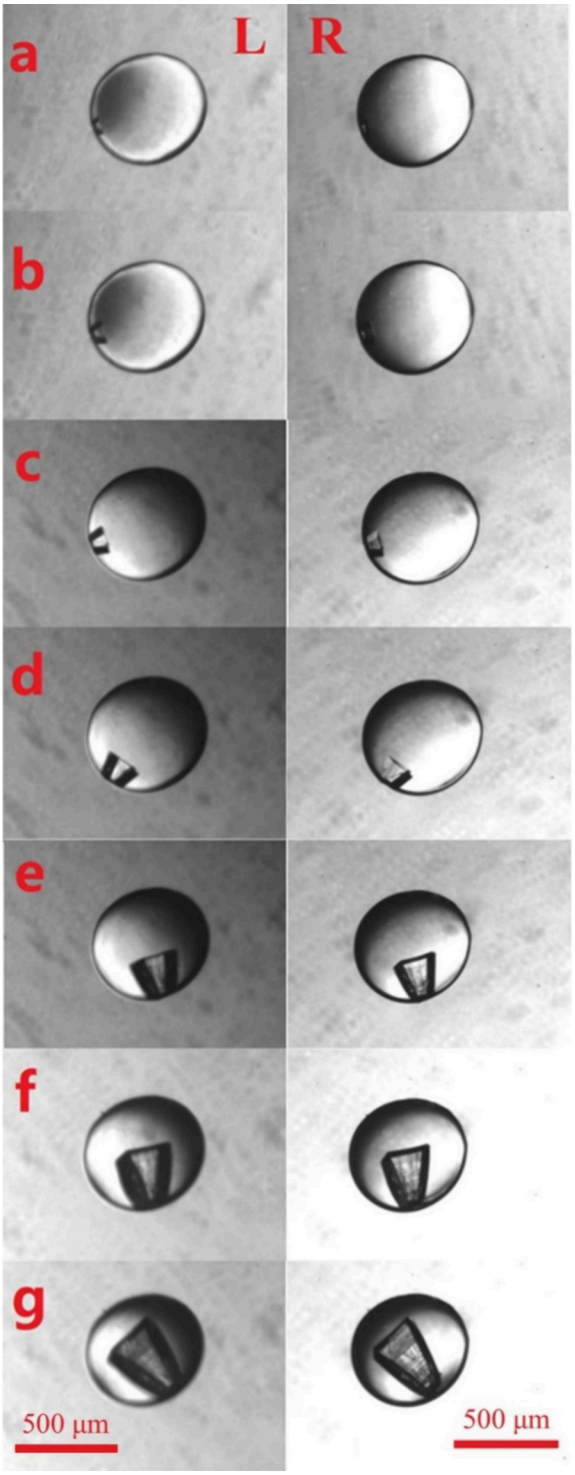

Figure 4. Growth process of α-LM taken by two cameras: *L* is left camera, *R* is right camera, and the images of the same crystal at different times (a−g, Red scale bar, 500 μm).

After image processing and 3D reconstruction, the change of axial growth dimensions of α-LM in the droplet against time *t* is shown in Figure 5a. From Figure 5a, with increasing time *t*, the growth of α-LM in the *a* and *b* axis directions increased gradually and then slowed because σ of α-LM decreased the growth driving force. The growth of α-LM in the *c*-axis direction almost stagnated after about 150 min after nucleation because the density of droplets was greater than that of kerosene, which was not suspended in the dispersed phase. Therefore, the α-LM grew close to the bottom of the beaker, and supersaturation in the *c*-axis direction was rapidly consumed after 150 min.

As shown in eqs 11-13), the key dimensions obtained from 3D reconstruction were used to calculate the areas of the (010) crystal plane, $(0\bar{1}0)$ crystal plane, and $(0\bar{1}1)$ crystal plane at different times *t*, respectively (Figure 5b). The results showed that the area of the crystal plane increased with the increase of the growth time *t*, but the growth of the crystal plane $(0\bar{1}0)$ almost stagnated after about 150 min. In addition, the crystal plane $(0\bar{1}0)$ was close to the edge of the droplets, and the growth of α-LM was closer to the capsule wall. Therefore, the mass transfer was not smooth, and the local supersaturation σ of the solution tended to 0, affecting the continued growth of the $(0\bar{1}0)$ crystal face. According to eq 11, the volume of α-LM at different *t* in the droplets was calculated with the area of the (010) crystal plane, $(0\bar{1}0)$ crystal plane, and $(0\bar{1}1)$ crystal plane, respectively. The real-time mass of α-LM could be calculated by multiplying it with $\rho_{\alpha\text{-LM}}$. As shown in Figure 5c, the volume and mass of α-LM precipitated from the solution gradually increased, but the increase rate gradually decreased. It is ascribed that the driving force of crystal growth was weakened because σ of the α-LM aqueous solution in the droplets was continuously consumed. After determining the relationship between the size and time of α-LM growth, the real-time concentration and real-time supersaturation σ of α-LM solution in the droplets were calculated as eqs 16 and 17. As shown in Figure 5d, with the increase of precipitation of α-LM crystals, the concentration and σ of the solutions decreased gradually, but the decrease of σ was about 4 times faster than that of the concentration. The results demonstrated the relationship between the growth rate of α-LM and σ against growth time *t*, and studying the in situ growth kinetics of α-LM is necessary.

3.6. Kinetics of 3D Axial Growth of α-LM. The relationship between the axial growth rate of α-LM with *t* in droplets and supersaturation is shown in Figure 6. It is obvious that there is a significant monotonically decreasing nonlinear relationship between the axial growth rate and crystal area growth rate of α-LM crystal with the growth time *t* in droplets. From Figure 6, the correlation coefficient R^2, obtained from $G = kt^n$ is 0.8369, which is lower than the R^2, obtained from $G = ke^{nt}$, indicating that the latter is more suitable for describing the relationship between α-LM crystal growth and time *t* in the droplets. The unit cell is the basic repeating unit of the crystal structure, and *a*, *b*, and *c* represent the axes of the unit cell in three mutually perpendicular directions. Through experimental measurement methods and data analysis, the growth rate of the crystal along the *a*, *b*, and *c* axes during the crystal growth process is determined. In this study, the growth rate along the *a*-axis is fastest, and the growth rate along the *b* and *c* axes is relatively slow, so the crystal would preferentially grow along the *a*-axis to form a specific crystal shape.

The growth rate and time variation of α-LM on each axis were fitted with Origin software. The red curve was the best fitting light curve model, and the fitting results are shown in Figure 6. The growth relationship and R^2 are calculated as,

Size growth rate in the *a*-axis direction:

$$G_{a\text{-axis}} = 96.0196e^{-0.00722t}, \quad R^2 = 0.8741 \tag{18}$$

https://doi.org/10.1021/acsomega.4c10746
ACS Omega 2025, 10, 10493−10505

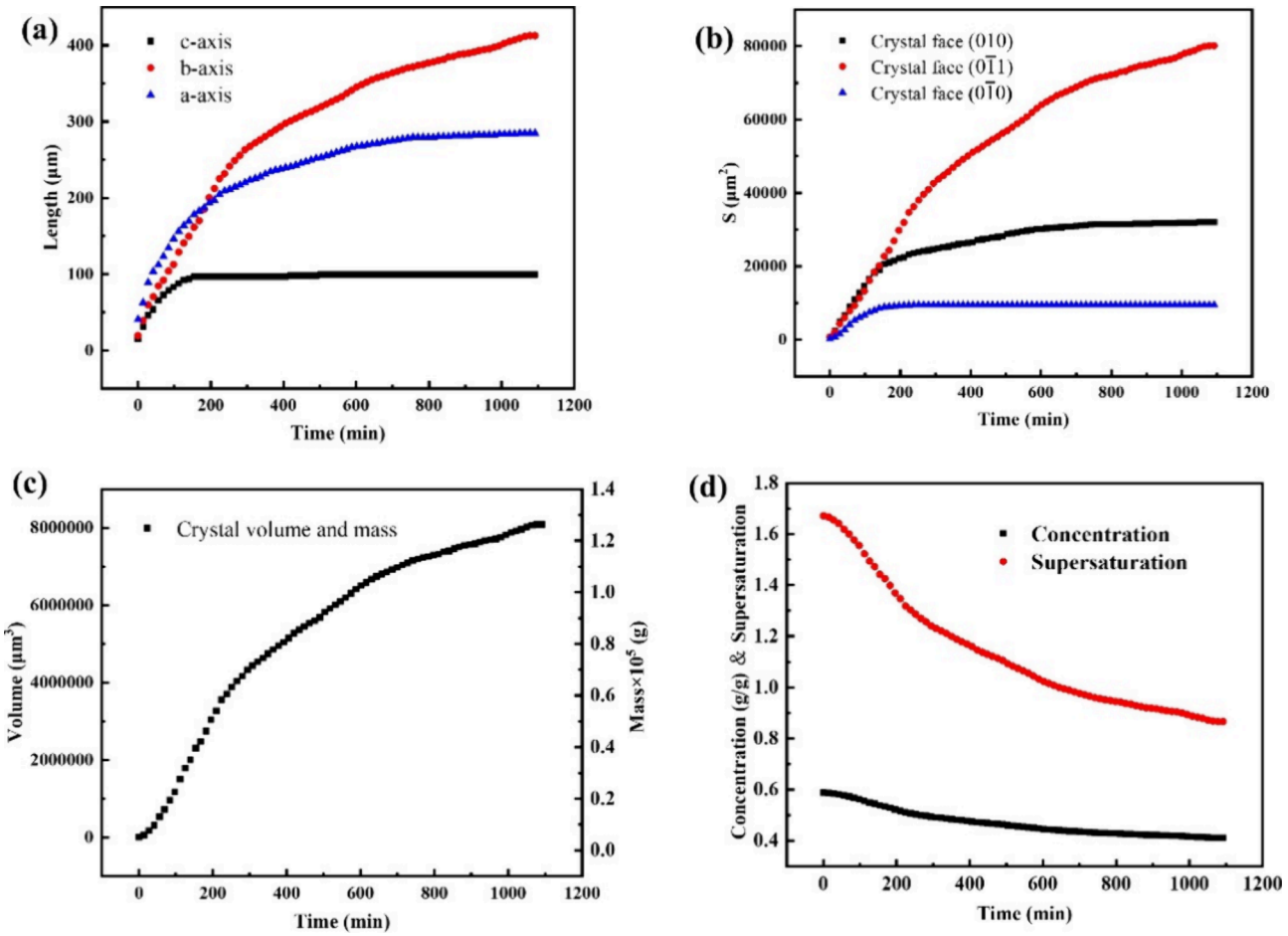

Figure 5. α-LM against t in droplet: Variation diagram of 3D axial growth length of α-LM with t (a). Variation diagram of area of α-LM face (010), (0$\bar{1}$0) and (0$\bar{1}$1) with t (b). Variation diagram of α-LM volume and mass in microdroplet with t (c). Variation diagram of concentration and supersaturation of α-LM in droplet with t (d).

Size growth rate in the b-axis direction:

$$G_{b\text{-axis}} = 73.1382e^{-0.00299t}, \quad R^2 = 0.8170 \tag{19}$$

Size growth rate in the c-axis direction:

$$G_{c\text{-axis}} = 89.6688e^{-0.01545t}, \quad R^2 = 0.9469 \tag{20}$$

Based on the empirical equation ($G = K\sigma^n$), where G is the crystal growth rate, K is a constant related to factors like temperature and surface properties of the crystal, and n is the crystal growth order.[35] When $n = 1$, first-order growth indicates that the crystal growth process is mainly controlled by solute diffusion and the growth rate against supersaturation relation is almost linear, implying that the crystal growth rate is determined by solute molecules diffuse from the solution to the crystal surface. When $n > 1$, the growth rate is related to the square or higher power of the supersaturation, indicating a more complex growth process. The process may involve the more complex stages, such as adsorption and aggregation of solutes on the crystal surface.

The power exponential function is used to establish the relationship between the axial growth rates of α-LM and σ. The fitted curves are shown in Figure 6a−g. The corresponding kinetic models and R^2 are as follows,

Growth kinetic equation in the a-axis direction:

$$G_{a\text{-axis}} = 2.7757\sigma^{6.5628}, \quad R^2 = 0.8717 \tag{21}$$

Growth kinetic equation in the b-axis direction:

$$G_{b\text{-axis}} = 12.1972\sigma^{3.4619}, \quad R^2 = 0.7960 \tag{22}$$

Growth kinetic equation in the c-axis direction:

$$G_{c\text{-axis}} = 0.0158\sigma^{16.3109}, \quad R^2 = 0.9433 \tag{23}$$

Based on the fitting kinetic models, the growth process of α-LM in the a-axis direction was between the sixth-order growth and the seventh-order growth, the b-axis growth process was between the third-order growth and the fourth-order growth, and the c-axis growth process was greater than the tenth-order growth, which is dependent on the solution supersaturation.

3.7. Kinetics of Crystal Plane Growth of α-LM. α-LM exists in the form of hexahedral flake crystals at room temperature. This crystal structure is maintained by hydrogen bonds and van der Waals forces between its molecules. α-LM molecules interact through hydrogen bonds to form a stable lattice structure, in which each molecule is arranged in a specific way with the surrounding molecules to minimize the free energy of the system.[36,37] After 3D image reconstruction to determine the key size of α-LM, the area of all crystal planes and their relationship with t and supersaturation could be calculated theoretically. Taking the (010) plane, (0$\bar{1}$0) plane, and (0$\bar{1}$1) plane of α-LM crystal as examples, the change of the crystal plane area with time t is shown in Figure 5, and the

https://doi.org/10.1021/acsomega.4c10746
ACS Omega 2025, 10, 10493−10505

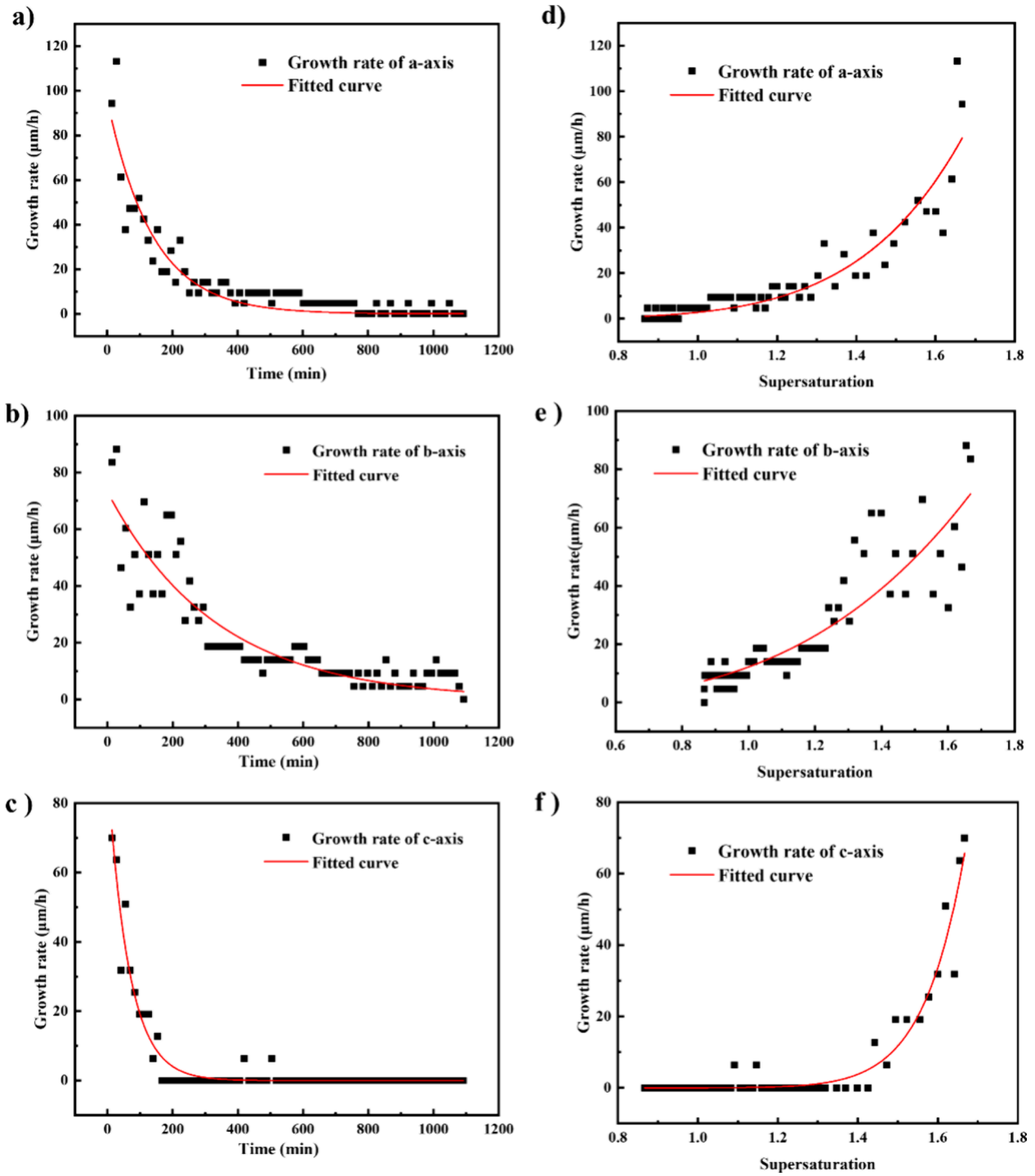

Figure 6. 3D axial growth rate of the α-LM crystal with t (a–c) and supersaturation (d–f) in the droplet.

relationship between the growth rate and growth time t and σ is shown in Figure 7.

The relationship between the growth rate and growth time of the (010) plane, $(0\bar{1}0)$ plane, and $(0\bar{1}1)$ plane of α-LM was determined by fitting and R^2 areas, and the curves are shown in Figure 7a–c:

Growth rate–time relationship of (010) crystal plane:

$$G_{S_{(010)}} = 11363.4398e^{-0.00608t}, \quad R^2 = 0.8670 \tag{24}$$

Growth rate–time relationship of $(0\bar{1}0)$ crystal plane:

$$G_{S_{(0\bar{1}0)}} = 5633.1423e^{-0.00845t}, \quad R^2 = 0.7907 \tag{25}$$

Growth rate–time relationship of $(0\bar{1}1)$ crystal plane:

$$G_{S_{(0\bar{1}1)}} = 10511.1024e^{-0.00188t}, \quad R^2 = 0.7467 \tag{26}$$

Based on the empirical formula ($G = K\sigma^n$), the models of σ of the α-LM crystal (010), $(0\bar{1}0)$, and $(0\bar{1}1)$ and solution in the droplets were established, respectively, and the fitted curves are shown in Figure 7d–f:

https://doi.org/10.1021/acsomega.4c10746
ACS Omega 2025, 10, 10493–10505

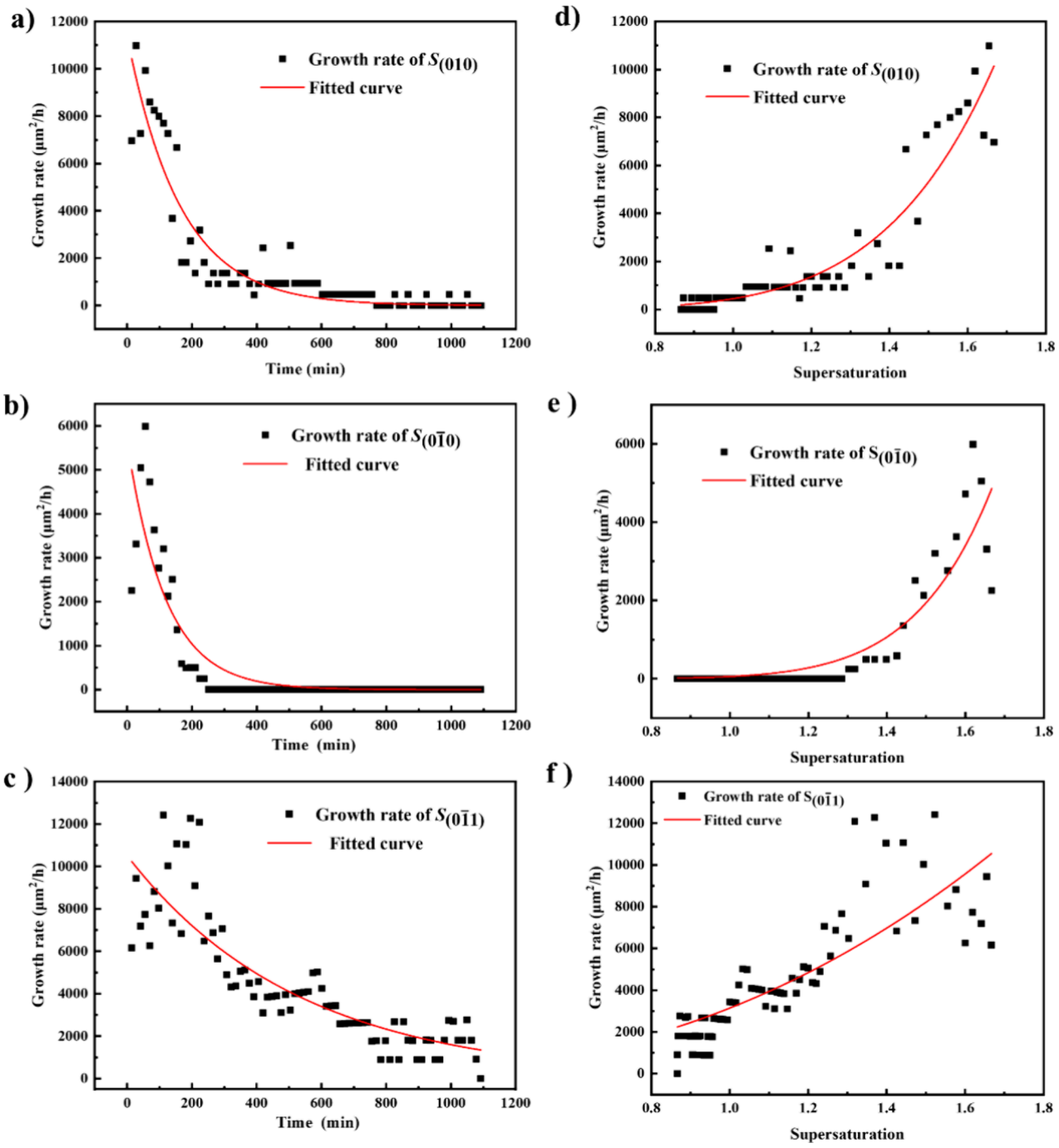

Figure 7. Growth rate of α-LM crystal face (010), $(0\bar{1}0)$, and $(0\bar{1}1)$ with t (a–c) and σ (d–f) in the droplet.

Growth rate–σ relationship of (010) crystal plane:

$$G_{S_{(010)}} = 445.5256\sigma^{6.1153}, \quad R^2 = 0.8934 \tag{27}$$

Growth rate–σ relationship of $(0\bar{1}0)$ crystal plane:

$$G_{S_{(0\bar{1}0)}} = 57.3127\sigma^{8.6883}, \quad R^2 = 0.8339 \tag{28}$$

Growth rate–σ relationship of $(0\bar{1}1)$ crystal plane:

$$G_{S_{(0\bar{1}1)}} = 3144.8259\sigma^{2.3680}, \quad R^2 = 0.6748 \tag{29}$$

The series principle of crystal growth mainly involves the relationship between the growth rate of α-LM and σ. The overall growth pattern in this study is parabolic. Based on the kinetic equation obtained by the fitting results, the growth process of α-LM crystal plane (010) in the droplet was between the sixth-order growth and the seventh-order growth, as well as the crystal plane $(0\bar{1}0)$. However, the growth process of the crystal plane $(0\bar{1}1)$ was between the secondary growth and the tertiary growth, which was due to its consumption of more σ. At low σ, the integration of particles into the surface is a controlling step of crystal growth, forming smooth faces of polyhedral crystals. Under the nonclassical crystal growth framework, the crystal growth rate is not only related to the addition of monomers, but also to the collision and aggregation of other particles. This growth mode is more significant at high σ. The results indicated that the crystal

https://doi.org/10.1021/acsomega.4c10746
ACS Omega 2025, 10, 10493−10505

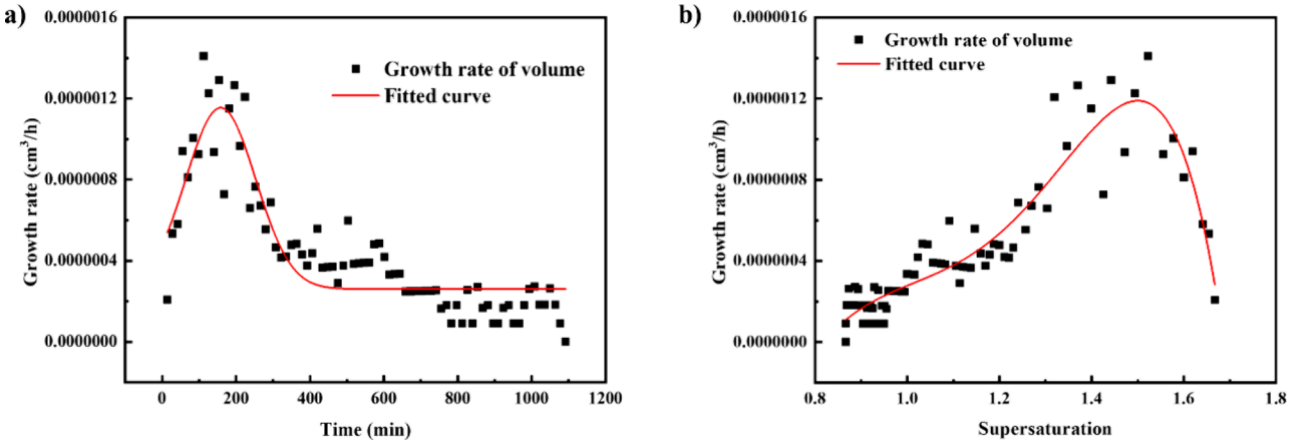

Figure 8. Relationship between volume growth rate with t (a) and supersaturation (b) of the α-LM crystal in the droplets.

growth rate is proportional to the higher power of σ, implying an exponential relationship, that is, a localized strengthening effect.

3.8. Volume Growth Kinetics of the α-LM Crystal. According to eq 14, the volume growth rates of α-LM in the droplets and time t and supersaturation σ were calculated with the area and edge size of (010) plane, $(0\bar{1}0)$ plane, and $(0\bar{1}1)$ plane, and the results are shown in Figure 8. In the process of solution crystallization, an increase in σ usually leads to faster nucleation and growth rates, which is usually controlled by σ of the solution. In addition, crystal growth is a dynamic process, and the crystal volume gradually increases with increasing t. In a certain range of σ, the growth rates could increase first and then stabilize against t, and the solute concentration in the solution gradually decreases, resulting in a decrease in σ. The growth inhibition phenomenon that may occur during the process of crystal growth would affect the change in growth rate against t. There are two reasons. (1) Diffusion limitation: at high supersaturation, the solute concentration gradient in the solution increases, but the diffusion rate of the solute may not be able to keep up with the demand for crystal growth. The solute near the crystal surface is quickly consumed, while the solute far away has no time to replenish, which limits the further growth of the crystal and reduces the growth rate.[38] (2) Surface energy change: as the crystal grows, its surface area continues to increase, and the surface energy also increases accordingly. At high σ, the surface energy may reach a critical value, making the crystal growth unstable and the growth rate reduced.[39]

$$G_{\text{volume}} = 2.6033 \times 10^{-7} + 8.94 \times 10^{-7} e^{-0.5\left(\frac{t-158.358}{94.5576}\right)^2}, \quad R^2 = 0.8012 \tag{30}$$

$$G_{\text{volume}} = 7.08 \times 10^{-6} - 7.13 \times 10^{-5}\sigma + 1.96 \times 10^{-4}\sigma^2 - 2.33 \times 10^{-4}\sigma^3 + 1.28 \times 10^{-4}\sigma^4 - 2.65 \times 10^{-5}\sigma^5, \quad R^2 = 0.8727 \tag{31}$$

Determining the crystal growth rate from a volumetric perspective can more comprehensively reflect the growth of crystals in three-dimensional space. A single peak nonlinear relationship was observed between the volume growth rate of α-LM with t and solution σ in the microdroplets, and the Guass-Amp model was used to fit the relationship, and the results were shown in eq 30. The solution σ relationship was fitted using a fifth order polynomial, and the result was shown in eq 31. According to the volume growth dynamics model, it can be inferred that the α-LM droplets saturated at 60 °C, and then they are cooled to 25 °C. The growth rate of α-LM crystals is the fastest within 100−150 min after nucleation, and the corresponding solution supersaturation σ is about 1.5. The 3D observation of the morphology and the fitting results show that the nucleus volume of α-LM is about 7.08×10^{-6} cm^3. The fitting polynomial coefficients also indicated that the growth process of α-LM crystals in the microdroplets was mainly between second-order growth and fourth-order growth (Figure 9).

3.9. Physical and Chemical Significance of the α-LM Crystal. Based on the above results, real-time monitoring of the growth process of α-LM crystals in the microdroplets could avoid interference and damage to the sample and reflect the natural growth of the crystal more truly. In situ detection of the crystal axis and crystal plane growth of α-LM in microdroplets has important physical and chemical significance: (1) Understand the crystal growth mechanism, reveal the nucleation and growth laws of α-LM in a microdroplet environment, and clarify the growth rate and method of the crystal axis and crystal plane; (2) Optimize the crystallization process, regulate the crystallization process to give key parameters, and optimize crystallization conditions such as temperature, humidity, and solution concentration accordingly. The growth characteristics of α-LM can help in the prediction of the crystal transformation of lactose in pharmaceutical preparations and ensure the stability and dissolution of drugs. They can provide references for studying the growth of other hydrate crystals or similar systems.

4. CONCLUSIONS

This study introduced microfluidics into microdroplets to produce uniform crystals. The saturated liquid was divided into monodisperse droplets and further crystallized in a constant-temperature-controlled crystallizer to observe the in situ growth process of the crystal. It provides a new scientific basis and method for the theoretical and applied research on the controllability of crystal form and process intensification in crystallization separation and has guiding significance for the industrial production and application of lactose. The law of continuous preparation of W/O type droplets by a self-designed microfluidic chip was summarized, and the

https://doi.org/10.1021/acsomega.4c10746
ACS Omega 2025, 10, 10493−10505

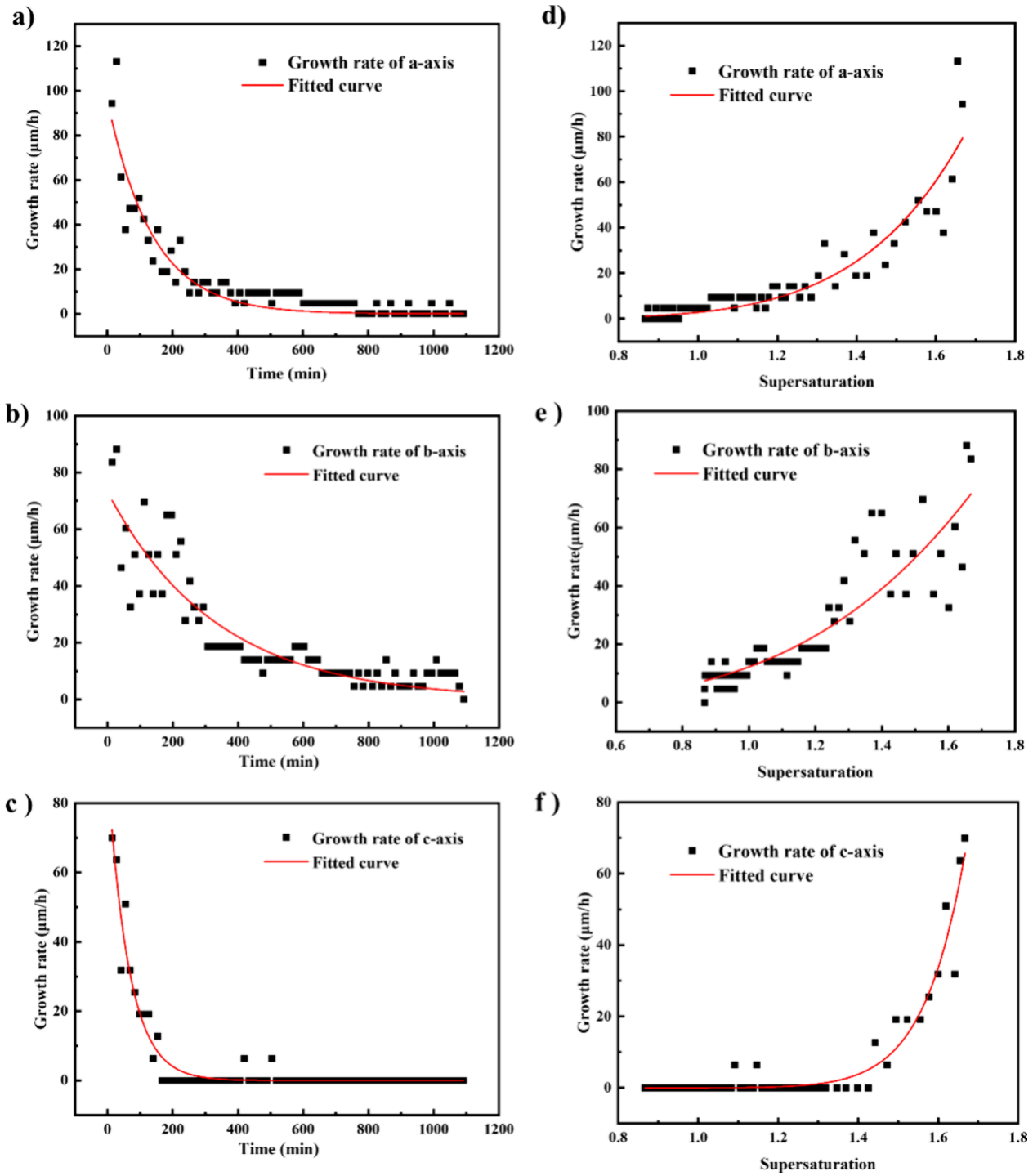

Figure 9. 3D axial growth rate of α-LM with time t (a–c) and supersaturation (d–f) in the droplet.

morphology of α-LM under finite domain conditions was reasonably approximated with a regular geometry (prism), providing a method for calculating the real-time concentration and supersaturation of α-LM solution in microdroplets. The paired in situ growth images of α-LM were taken by dual cameras, and the three-dimensional axial size, crystal area, and volume of α-LM at different t were determined by 3D reconstruction technology, and the kinetic equation of volume growth rate was calculated in turn. The results show that the growth process of α-LM in droplets is mainly between secondary growth and quaternary growth, achieving the application effect of confined domain enhanced crystal growth, which has guiding significance for crystallization theory research and lactose industrial production.

■ ASSOCIATED CONTENT

Supporting Information

The Supporting Information is available free of charge at https://pubs.acs.org/doi/10.1021/acsomega.4c10746.

α-LM droplets: schematic and diagram of the device; the pictures were taken by the author *Guan Youliang;* imaging steps for reconstructing the 3D shape of

https://doi.org/10.1021/acsomega.4c10746
ACS Omega 2025, 10, 10493−10505

crystals; the effect of the different inner phase flow rates on W/O droplet formation: high-speed camera images, and the formation of droplets; the effect of the different outer fluid flow rates on W/O droplet formation: high-speed camera images, and the formation of droplets; crystallographic data of a-LM crystals (PDF)

AUTHOR INFORMATION

Corresponding Author

Zujin Yang − *School of Chemical Engineering and Technology, Sun Yat-Sen University, Zhuhai 510275, China;* orcid.org/0000-0003-2319-3055; Email: yangzj3@mail.sysu.edu.cn

Authors

Youliang Guan − *School of Chemical Engineering and Technology, Sun Yat-Sen University, Zhuhai 510275, China; Kunming Branch of the 705 Research Institute, China State Shipbuilding Corporation Limited, Kunming 650032, China*

Yanqin Cai − *School of Chemical Engineering and Technology, Sun Yat-Sen University, Zhuhai 510275, China*

Jingqin Jiang − *School of Chemical Engineering and Technology, Sun Yat-Sen University, Zhuhai 510275, China*

Complete contact information is available at: https://pubs.acs.org/10.1021/acsomega.4c10746

Author Contributions

Z.Y. conceived the idea, reviewed the manuscript, and contributed to funding acquisition, Y.G. contributed to original draft, compilation, and discussion of results, Y.C. contributed to manuscript revision, and J.J. contributed to the simulation. Y.G. and Y.C. are contributed equally to this work.

Notes

The authors declare no competing financial interest.

ACKNOWLEDGMENTS

The authors gratefully acknowledge the National Natural Science Foundation of China (22378435) and Guangdong Basic and Applied Basic Research Foundation (2022A1515140008).

REFERENCES

(1) Sánchez-García, Y. I.; Gutiérrez-Méndez, N.; Landeros-Martínez, L. L.; Ramos-Sánchez, V. H.; Orozco-Mena, R.; Salmerón, I.; Leal-Ramos, M. Y.; Sepúlveda, D. R. Crystallization of Lactose−Protein Solutions in the Presence of Flavonoids. *J. Agr. Food Chem.* **2022**, *70*, 2684−2694.

(2) Uald Lamkaddam, I.; Vega, E.; Colón, J.; Ponsá, S.; Llenas, L.; Mora, M. Progressive freeze concentration of cheese whey for protein and lactose recovery. *Int. Dairy. J.* **2023**, *139*, No. 105572.

(3) Batra, A.; Desai, D.; Serajuddin, A. T. M. Conversion of α-lactose monohydrate to anhydrous form with superior tabletability by twin-screw extrusion at elevated temperature. *Int. J. Pharm.* **2020**, *588*, No. 119790.

(4) Hayashi, M.; Shichiri, T. Theoretical and experimental study of the growth of perfect crystals. *J. Cryst. Growth.* **1974**, *21*, 254−260.

(5) Kurihara, K.; Miyashita, S.; Sazaki, G.; Nakada, T.; Suzuki, Y.; Komatsu, H. J. J. O. C. G. Interferometric study on the crystal growth of tetragonal lysozyme crystal. *J. Cryst. Growth.* **1996**, *166*, 904−908.

(6) Wijayasinghe, R.; Bogahawaththa, D.; Chandrapala, J.; Vasiljevic, T. Crystallization behavior and crystal properties of lactose as affected by lactic, citric, or phosphoric acid. *J. Dairy. Sci.* **2020**, *103*, 11050−11061.

(7) Altamimi, M. J.; Wolff, K.; Nokhodchi, A.; Martin, G. P.; Royall, P. G. Variability in the α and β anomer content of commercially available lactose. *Int. J. Pharm.* **2019**, *555*, 237−249.

(8) Lara-Mota, E. E.; Nicolás-Vázquez, M. I.; López-Martínez, L. A.; Espinosa-Solis, V.; Cruz-Alcantar, P.; Toxqui-Teran, A.; Saavedra-Leos, M. Z. Phenomenological study of the synthesis of pure anhydrous β-lactose in alcoholic solution. *Food Chem.* **2021**, *340*, No. 128054.

(9) Dombrowski, R. D.; Litster, J. D.; Wagner, N. J.; He, Y. Crystallization of alpha-lactose monohydrate in a drop-based microfluidic crystallizer. *Chem. Eng. Scie.* **2007**, *62*, 4802−4810.

(10) Parimaladevi, P.; Srinivasan, K. Achievement of favorable uniform crystal size distribution of alpha-lactose monohydrate (α-LM) through swift cooling process. *J. Food Eng.* **2015**, *151*, 1−6.

(11) Dincer, T. D.; Ogden, M. I.; Parkinson, G. M. In situ investigation of growth rates and growth rate dispersion of α-lactose monohydrate crystals. *J. Cryst. Growth.* **2009**, *311*, 1352−1358.

(12) Martins, P. M.; Rocha, F. A.; Rein, P. J. C. G. Design, The Influence of Impurities on the Crystal Growth Kinetics According to a Competitive Adsorption Model. *Cryst. Growth Des.* **2006**, *6*, 2814−2821.

(13) Huo, Y.; Liu, T.; Yang, Y.; Ma, C. Y.; Wang, X. Z.; Ni, X. In Situ Measurement of 3D Crystal Size Distribution by Double-View Image Analysis with Case Study on l-Glutamic Acid Crystallization. *Ind. Eng. Chem. Res.* **2020**, *59*, 4646−4658.

(14) Szilágyi, B.; Eren, A.; Quon, J. L.; Papageorgiou, C. D.; Nagy, Z. K. Monitoring and digital design of the cooling crystallization of a high-aspect ratio anticancer drug using a two-dimensional population balance model. *Chem. Eng. Sci.* **2022**, *257*, No. 117700.

(15) Zheng, Y.; Wang, X.; Wu, Z. Machine Learning Modeling and Predictive Control of the Batch Crystallization Process. *Ind. Eng. Chem. Res.* **2022**, *61*, 5578−5592.

(16) Olbert, M.; Nedela, V.; Jirak, J.; Hudec, J. Size and shape analysis of micro- to nano-particles of quartz powders using advanced electron microscopy and laser diffraction methods. *Powder. Technol.* **2024**, *433*, No. 119250.

(17) Cheng, H.-J.; Hsu, C.-H.; Hung, C.-L.; Lin, C.-Y. A review for cell and particle tracking on microscopy images using algorithms and deep learning technologies. *Biomed. J.* **2022**, *45*, 465−471.

(18) Zong, S.; Zhou, G.; Li, M.; Wang, X. Deep learning-based on-line image analysis for continuous industrial crystallization processes. *Particuology.* **2023**, *74*, 173−183.

(19) Wang, L.; Shirodkar, S. N.; Zhang, Z.; Yakobson, B. I. Defining shapes of two-dimensional crystals with undefinable edge energies. *Nat. Comput. Sci.* **2022**, *2*, 729−735.

(20) Larsen, P. A.; Rawlings, J. B.; Ferrier, N. J. An algorithm for analyzing noisy, in situ images of high-aspect-ratio crystals to monitor particle size distribution. *Chem. Eng. Sci.* **2006**, *61*, 5236−5248.

(21) Zhang, R.; Ma, C. Y.; Liu, J. J.; Wang, X. Z. On-line measurement of the real size and shape of crystals in stirred tank crystalliser using non-invasive stereo vision imaging. *Chem. Eng. Sci.* **2015**, *137*, 9−21.

(22) Jin, Y.; Li, Q.; Jiang, D.; Tong, R. High-fidelity 3D face reconstruction with multi-scale details. *Pattern. Recogn. Lett.* **2022**, *153*, 51−58.

(23) Duran, M.; Serrano, A.; Nikulin, A.; Dauvergne, J.-L.; Derzsi, L.; Palomo del Barrio, E. Microcapsule production by droplet microfluidics: A review from the material science approach. *Mater. Design.* **2022**, *223*, No. 111230.

(24) Seemann, R.; Brinkmann, M.; Pfohl, T.; Herminghaus, S. Droplet based microfluidics. *Rep. Prog. Phys.* **2012**, *75*, No. 016601.

(25) Jiang, Z.; Shi, H.; Tang, X.; Qin, J. Recent advances in droplet microfluidics for single-cell analysis. *Trac-trend. Anal. Chem.* **2023**, *159*, No. 116932.

(26) Rein, C.; Toner, M.; Sevenler, D. Rapid prototyping for high-pressure microfluidics. *Sci. Rep.* **2023**, *13*, 1232.

(27) Hwang, J.-H.; Hong, J.-S.; Oh, C.-W.; Joe, M.-J.; Jeong, H.-C.; Park, H.-G. Soft imprint lithography for liquid crystal alignment using

a wrinkled UVO-treated PDMS transferring method. *J. Mol. Liq.* **2021**, *323*, No. 115150.
(28) Bariki, S. G.; Movahedirad, S. Hydrodynamic characteristics of core/shell microdroplets formation: Map of the flow patterns in double-T microchannel. *Chem. Eng. J.* **2024**, *479*, No. 147749.
(29) Parimaladevi, P.; Srinivasan, K. Influence of supersaturation level on the morphology of α-lactose monohydrate crystals. *Int. Dairy. J.* **2014**, *39*, 301−311.
(30) Guan, Y.; Yang, Z.; Wu, K.; Ji, H. Crystallization Thermodynamics of α-Lactose Monohydrate in Different Solvents. *Pharmaceutics.* **2022**, *14*, 1774.
(31) Pisponen, A.; Pajumägi, S.; Mootse, H.; Sats, A.; Poikalainen, V.; Karus, A. Effect of cooling rates and low crystallization temperatures on morphology of lactose crystals obtained from Ricotta cheese whey. *Agron. Res.* **2014**, *12*, 787−792.
(32) Ulrich, J.; Frohberg, P. Problems, potentials and future of industrial crystallization. *Front. Chem. Sci. Eng.* **2013**, *7*, 1−8.
(33) Nielsen, A. E. Electrolyte crystal growth mechanisms. *J. Cryst. Growth* **1984**, *67*, 289−310.
(34) McDonald, E. J.; Turcotte, A. L. Density and refractive indices of lactose solutions. *J. Res. Natl. Bur. Stand.* **1948**, *41*, 63−68.
(35) Miura, H. Crystal growth hysteresis in spiral growth. *Cryst. Growth. Des.* **2020**, *20*, 245−254.
(36) Newburg, D. S.; Chen, C.; Wiederschain, G., *CHAPTER 32: Analysis of Human Milk Lactose*; The Royal Society of Chemistry, 2012; pp 570−588.
(37) Wong, S. Y.; Hartel, R. W. Crystallization in lactose refining-a review. *J. Food Sci.* **2014**, *79*, R257−R272.
(38) Howell, T. A.; Ben-Yoseph, E.; Rao, C.; Hartel, R. W. Sucrose Crystallization Kinetics in Thin Films at Elevated Temperatures and Supersaturations. *Cryst. Growth Des.* **2002**, *2* (1), 67−72.
(39) Vlieg, E. The role of surface and interface structure in crystal growth. *Prog. Cryst. Growth Charact. Mater.* **2016**, *62* (2), 203−211.

https://doi.org/10.1021/acsomega.4c10746
ACS Omega 2025, 10, 10493−10505